Nano Materials Science 6 (2024) 794–804

Contents lists available at ScienceDirect

Nano Materials Science

journal homepage: www.keaipublishing.com/cn/journals/nano-materials-science/

Manipulating polarization attenuation in NbS_2–NiS_2 nanoflowers through homogeneous heterophase interface engineering toward microwave absorption with shifted frequency bands

Yiru Fu [a], Yuping Wang [a], Junye Cheng [b,*], Yao Li [a], Jing Wang [a], Yongheng Jin [d], Deqing Zhang [a,**], Guangping Zheng [c], Maosheng Cao [d,***]

[a] School of Materials Science and Engineering, Qiqihar University, Qiqihar, 161006, China
[b] Department of Materials Science, Shenzhen MSU-BIT University, Shenzhen, Guangdong Province, 517182, China
[c] Department of Mechanical Engineering, Hong Kong Polytechnic University, Hung Hom, Kowloon, China
[d] School of Materials Science and Engineering, Beijing Institute of Technology, Beijing, 100081, China

ARTICLE INFO

Keywords:
Interface engineering
Electromagnetic wave absorption
Heterostructures
Interfacial polarization

ABSTRACT

Homogeneous heterogeneous (heterophase) interfaces regulated with low energy barriers have a fast response to applied electric fields and could provide a unique interfacial polarization, which facilitate the transport of electrons across the substrate. Such regulation on the interfaces is effective in modulating electromagnetic wave absorbing materials. Herein, we construct NbS_2–NiS_2 heterostructures with NiS_2 nanoparticles uniformly grown in NbS_2 hollow nanospheres, and such particular structure enhances the interfacial polarization. The strong electron transfer at the interface promotes electron transport throughout the material, which results in less scattering, promotes conduct ion loss and dielectric polarization relaxation, improves dielectric loss, and results in a good impedance matching of the material. Consequently, the absorbing band may be successful tuned. By regulating the amount of NiS_2, the heterogeneous interface is finely alternated so that the overall wave-absorbing performance is shifted to lower frequencies. With a NiS_2 content of 15 wt% and an absorber thickness of 1.84 mm, the minimum reflection loss at 14.56 GHz is −53.1 dB, and the effective absorption bandwidth is 5.04 GHz; more importantly, the minimum reflection loss in different bands is −20 dB, and the microwave energy absorption rate reaches 99% when the thickness is about 1.5–4.5 mm. This work demonstrates the construction of homogeneous heterostructures is effective in improving the electromagnetic absorption properties, providing guideline for the synthesis of highly efficient electromagnetic absorbing materials.

1. Introduction

With the speedy growth of electronic technology as well as the large-scale application of electromagnetic equipment in various fields, the issues on electromagnetic interference and electromagnetic pollution are growing more and more serious [1–4]. The use of electromagnetic wave (EMW) absorbing materials is an excellent way to address the problems. Material that absorbs EMW can effectively convert the energy of EMW into thermal energy [5–7]. Recently, the EMW absorbing materials have been further developed to possess thinner thickness, lighter weight, wider bandwidth, and stronger reflection loss (RL). Among many new materials, heterostructure materials with abundant heterogeneous or heterophase interfaces have significantly enhanced interface polarization within the EMW absorbing materials [8–10]. The impedance matching can be effectively adjusted through modulating the heterogeneous interfaces, which has become a cornerstone for designing and research of cutting-edge EMW, and the solution to the problem of electromagnetic interference and pollution will no longer be far away in the future [11–13].

Transition metal disulfides (TMDs) are promising EMW absorbing materials with unique electronic structure. In particular, TMDs can be used to construct heterophane interfaces with other materials easily

* Corresponding author.
** Corresponding author.
*** Corresponding author.
E-mail addresses: chengjunye@smbu.edu.cn (J. Cheng), 00582@qqhru.edu.cn (D. Zhang), caomaosheng@bit.edu.cn (M. Cao).

https://doi.org/10.1016/j.nanoms.2024.05.003
Received 15 February 2024; Accepted 3 April 2024
Available online 14 July 2024

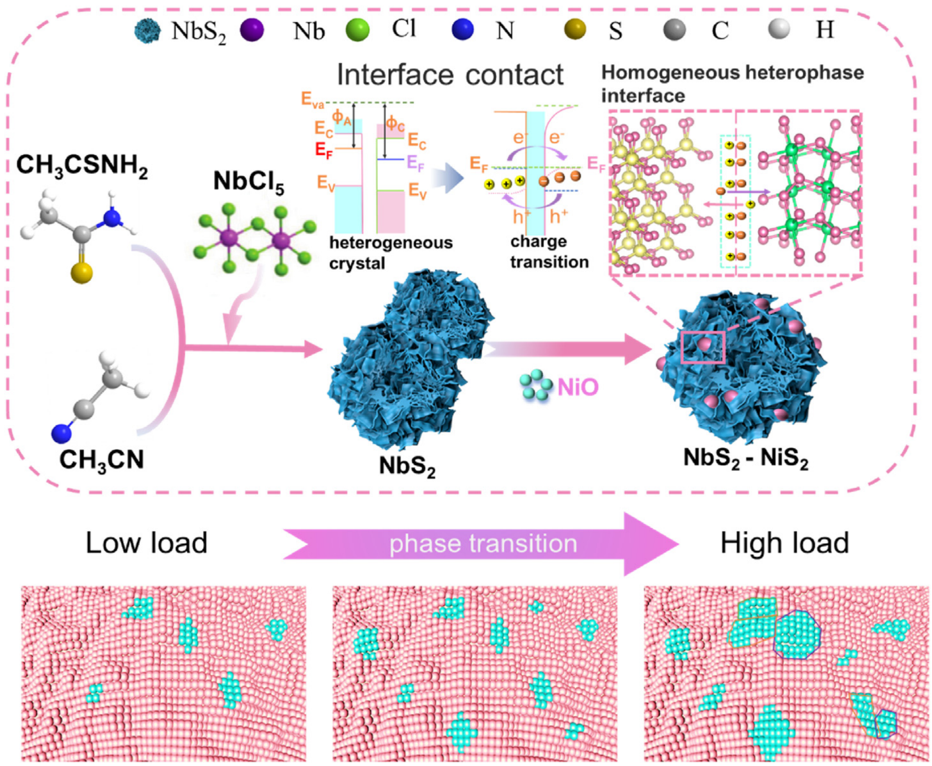

Fig. 1. Synthetic routes for the NbS_2–NiS_2 hybrids.

[14–17]. Compared with VIB group TMDs, NbS_2 is characterized by good conductivity, high dielectric loss, and abundant edge active sites [18–21]. Because of its hollow nanosphere structure formed by stacking nanosheets, NbS_2 has a large specific surface area conducive to the attenuation of EMW in the absorber. Thus, NbS_2 is considered to be an excellent EMW absorbing materials.

However, the sole loss mechanism for NbS_2 leads to undesirable properties such as large thickness for minimum reflection loss and poor impedance matching with some thicknesses, which limit its EMW absorption performance. The construction of heterostructures is one of the most effective ways that solve the problems mentioned above [22–25]. For example, Zhang's group hydrothermally synthesized WS_2 pleated sheets, and further constructed heterostructures on the basis of raw materials to obtain WS_2-rGO hybrids by hydrothermal method. Huang et al. synthesized VS_2 nanosheets and used them in electromagnetic wave absorbers. The VS_2/Co_3O_4 heterojunction was further embedded with Co_3O_4 on the surface and between the layers, and a series of experiments confirmed that these materials have good impedance matching and electromagnetic wave absorption properties [26–28]. Due to the construction of heterogeneous interfaces, the effective absorption bandwidth (EAB) of the absorber is significantly improved and the performance is enhanced [29]. Compared with EMW absorbing materials with a sole loss mechanism, the construction of heterogeneous interfaces can adjust the impedance matching, and their multiple loss mechanisms can meet the requirements of efficient microwave absorption [30]. However, the charge redistribution between heterogeneous interfaces formed between different materials phases generates a strong built-in electric field and produces a high energy barrier at the interface, leading to a significant limitation of free electron transport at the interface, which is not conducive to achieving high conduction losses in the sample. Unlike conventional interfaces constructed from two different materials, the homogeneous heterogeneity formed by the same type of materials minimizes the interfacial charge redistribution, and the low interfacial energy barriers will provide unique interfacial polarization, facilitating the scattering transport of electrons across the substrate. Under an applied electric field, the low energy barrier leads to fast responses of polarization of interfaces and promotes the improved impedance matching properties, which leads to superior wave-absorbing properties of the material. For example, amorphous/crystalline γ-Fe_2O_3 nanosheets were prepared by Wu et al. A low energy barrier was formed on both sides of the heterophane interface, which facilitated electron transport. The results showed that heterophane materials were promising microwave absorbers with high performance [31,32].

Nickel sulfide (NiS_2) is widely used in photocatalysis, environmental protection and energy fields because of its low density, good photovoltaic performance, environmental friendliness and stable chemical properties [33–38]. Since NiS_2 has excellent semiconductor properties, it is often incorporated with other materials to form heterostructures. The properties of the materials can be improved by the implementation of interfacial polarization between multiple phases of materials [39–42].

In this study, NbS_2–NiS_2 homogeneous heterostructures are synthesized by continuous solvothermal techniques. By adjusting the amount of NiS_2, the complex dielectric constant can be controlled and the heterogeneous interface can be finely tuned to endow the material with more homogeneous heterogeneous interface, and the wave-absorbing band is successfully modulated to shift toward a lower frequency. Furthermore, the strong electron shift at the interface increases the electrical conductivity of the material and improves the conduction loss, and the full contact between different phases at the heterophase interface produces a strong interfacial polarization, which enhances the electromagnetic wave loss (EMWL) capability of the material. The improvement of the microwave absorption properties of the NbS_2–NiS_2 heterostructures is attributed to the presence of abundant homogeneous heterogeneous interfaces that could enhance the interfacial polarization for electromagnetic wave absorption, an excellent impedance matching, excellent electrical conductivity, and their special three-dimensional hollow spherical structure.

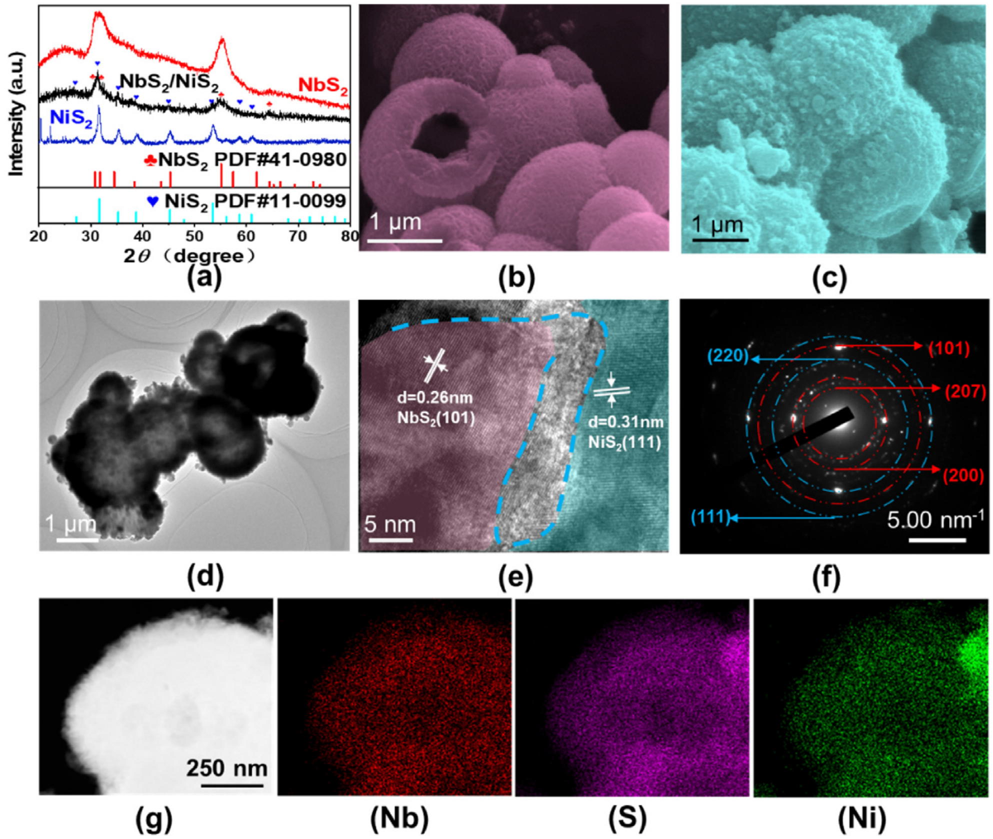

Fig. 2. (a) XRD patterns of NbS_2–NiS_2, NbS_2 and NiS_2, SEM image of (b) NbS_2 and (c) NbS_2–NiS_2-2, (d) TEM image of NbS_2–NiS_2-2, (e) HRTEM image of NbS_2–NiS_2-2, (f) SAED patterns of NbS_2–NiS_2-2 and (g) EDS mapping of NbS_2–NiS_2-2.

2. Experimental

2.1. Synthesis of NbS_2 nanoparticles

CH_3CSNH_2 is dissolved in 65 mL of CH_3CN and stirred for 10 min, then $NbCl_5$ is added to the mixture and stirred for 10 min to obtain a clear yellowish solution. The above process should be carried out as soon as possible to prevent the material from reacting with air. The remedy was moved to a kettle containing a 100 mL reactor lined with polytetrafluoroethylene, which was then sealed for the reaction at 210°C for a duration of 24 h. Subsequently, the reactor was allowed to cool down to room temperature on its own and was left undisturbed.

2.2. Synthesis of NbS_2–NiS_2 hybrids

Firstly, the cooled NbS_2 was stirred well on a magnetic stirring table and set aside (about 30 min). 0.0267 g of nickel oxide was weighed and added to the solution and stirred for 10 min on the stirring table to ensure that the material was well mixed. The 100 mL PTFE reactor with the homogeneous solution was then placed in a heating unit with magnetic stirring. The reaction temperature was maintained at 210°C for 4 h with constant stirring. The reactor is not removed until the heating unit has cooled to room temperature. The NbS_2–NiS_2 hybrids should be washed at least three times with deionized water and ethanol, and then dried in an oven. NbS_2–NiS_2 samples with different NiS_2 contents were prepared according to the above steps. The samples prepared with 10 wt%, 15 wt% and 17 wt% NiS_2 input were named NbS_2–NiS_2-1, NbS_2–NiS_2-2 and NbS_2–NiS_2-3, respectively.

2.3. Material and characterizations

Detailed information on all materials and test equipment can be found in Supporting Information.

3. Results and discussion

The schematic process for the fabrication of NbS_2–NiS_2 heterojunction is shown in Fig. 1. In this study, NbS_2 is synthesized by using $NbCl_5$ and CH_3CSNH_2 as the initial precursors, and CH_3CN is chosen as the solvent. Different ratios of NiO are injected into the cooled NbS_2 solution, which lead to the in-situ growth of NiO vulcanization on NbS_2, and the formation of NbS_2–NiS_2 homogeneous heterogeneous interfaces.

X-ray diffraction (XRD) was performed to study the physical phase and crystal structure of the synthesized materials. The XRD patterns are presented in Fig. 2a. The peaks at $2\theta = 14.8°$, $31.0°$, $31.9°$, $34.7°$, $55.3°$, $64.7°$, and $89.0°$ correspond to (JPCDS card No.41-0980) the (002), (100), (101), (102), (110), (200), and (207) crystallography planes of NbS_2, respectively [43]. Simultaneously, the diffraction peaks at $2\theta = 27.2°$, $31.6°$, $35.3°$, $38.8°$, $45.3°$, $53.8°$, and $61.2°$ belong to (111), (200), (210), (211), (220), (311), (230), and (321) planes of NiS_2 (JPCDS No. 11–0099) [44], respectively. The XRD results demonstrate the successful synthesis of NbS_2–NiS_2 heterostructure. Moreover, it is found that the attenuation of the diffraction peaks of NbS_2–NiS_2 may be related to the introduction of NiS_2, which is attributed to the decrease in the quality of NbS_2 crystals due to the increase in the defect density during the synthesis of hybrids from NbS_2 and NiS_2. The presence of defects on the surface of NbS_2 crystals may result in polarization of the surrounding surfaces, which improves wave-absorbing properties.

Fig. 2b-g shows the typical morphology and composition of NbS_2 and NbS_2–NiS_2. As illustrated in Fig. 2b, it can be clearly observed from the SEM image that NbS_2 has a hollow sphere structure consisting of lamellae stacked on top of each other, with sphere sizes ranging from 1.5 − 3.5 μm. The TEM image of NiS_2 (Fig. S1) indicates that NiS_2 has a spherical shape with a diameter of about 10–30 nm. The SEM image of NbS_2–NiS_2

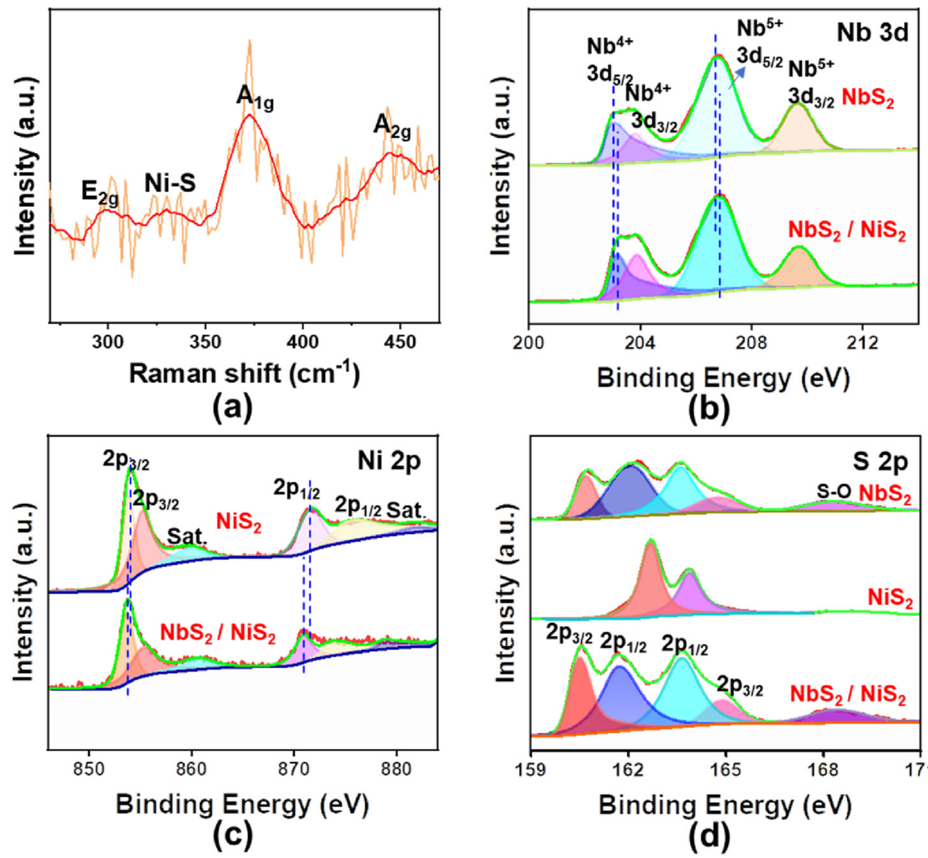

Fig. 3. (a) Raman spectrum of NbS_2–NiS_2-2, (b) Nb 3d XPS spectra of NbS_2 and NbS_2–NiS_2-2, (c) Ni 2p XPS spectra of NiS_2 and NbS_2–NiS_2-2 and (d) S 2p XPS spectra of NbS_2, NiS_2 and NbS_2–NiS_2-2.

(Fig. 2c) shows that it has a sphere shape with a diameter of about 3 μm, and there is a layer of small spheres with a diameter of about 30 nm on its surface, demonstrating the successful construction of NbS_2–NiS_2 heterostructures and the attachment of NiS_2 nanoparticles to the surface of NbS_2 nano hollow spheres. The TEM image in Fig. 1d also reveals that the large sphere has a hollow structure with many NiS_2 particles adhering to its surface. The TEM image in Fig. 2d shows the heterostructure similar to that in Fig. 1d. The high-resolution TEM (HR-TEM) images (Fig. 2c) of NbS_2–NiS_2 show clear bright and dark lattice stripes in different directions, with well-defined interfaces between them. The crystal planes with intervals of 0.28 nm and 0.31 nm belong to the (100) plane of NbS_2 and the (111) plane of NiS_2 [43], respectively, confirming the successful construction of NbS_2–NiS_2 heterostructures. Selected-area electron diffraction (SAED) patterns for NbS_2–NiS_2 (Fig. 2f) indicate that the diffraction ring is composed of the (100), (102) and (101) planes of NbS_2 and the (220) and (111) planes of NiS_2 [44], which are in good agreement with the XRD results. The results of XRD, SEM, TEM, HR-TEM and SAED demonstrate that both NbS_2 phase and NiS_2 phase could coexist in the NbS_2–NiS_2 samples. Therefore, the successful construction of NbS_2–NiS_2 heterostructure is confirmed. The elements Nb, S, and Ni are observed in the elemental mapping for the NbS_2–NiS_2 composites (Fig. 2g). The uniform distribution of Nb element in the large spheres and Ni element mainly concentrated on the small spheres in the upper right corner prove that NiS_2 nanoparticles are successfully implanted on NbS_2 surface.

In order to analyses the molecular structure information of the NbS_2–NiS_2-2 material, Raman test was performed on the sample. As shown in Fig. 3a, four peaks can be observed in the spectrum, where the peaks at 313, 378, and 449 cm^{-1} correspond to the characteristic peaks corresponding to the vibrations of NbS_2 in the E_{2g} is axisymmetric direction, and the out-of-plane vibrations of A_{1g} and A_{2g}, respectively. The peak at 345 cm^{-1}, on the other hand, corresponds to Ni–S [45,46], which is in agreement with previously reported results.

The NbS_2–NiS_2 heterostructure can be further investigated using photoelectron spectroscopy. As shown in Fig. 3(b–d), the carbon 1s signal at 284.8 eV is utilized for charge correction. As shown in Fig. S2c, typical peaks of Ni 2p, Nb 3d, and S 2p can be found in the wide-scan XPS spectra, which confirm the presence of Ni, Nb, and S elements in the NbS_2–NiS_2 heterostructure. The C, N, and O peaks shown in Fig. S2(a-c) are related to organic solvents. Fig. 3b shows the Nb 3d spectrum where the two peaks at 203.5 and 204.3 eV belong to Nb^{4+} $3d_{5/2}$ and $3d_{3/2}$, respectively [47,48]. The positive shift in the binding energy of NbS_2–NiS_2 compared to that of NbS_2 suggests that the construction of the NbS_2–NiS_2 heterostructure alters the surface electronic states of Nb 3d. In Fig. 3c, the double peaks at 854.1 and 871.9 eV can be attributed to Ni $2p_{3/2}$ and $2p_{1/2}$ of Ni 2p (Ni–S), suggesting the successful NiO vulcanization, whereas the two weaker peaks near 861.5 and 880.3 eV are oscillating satellite peaks [48–52]. A negative shift of the Ni $2p_{1/2}$ and Ni $2p_{3/2}$ peaks of NbS_2–NiS_2 can be observed compared to that ofNiS_2. The opposite shift in the binding energy is observed for the Nb 3d peak. The results indicate that due to the successful construction of the NbS_2–NiS_2 heterostructure, some electrons transfer from Nb to Ni, and there is a strong electronic interaction between NiS_2 and NbS_2. In the S 2p XPS spectra (Fig. 3b), the peaks at binding energies of 161.0 and 162.1 eV belong to S $2p_{3\ /2}$, and the peaks at 163.7 and 164.1 eV correspond to S $2p_{1\ /2}$, which can be assigned to the metal-sulfur bonding. The peak at 168.1 eV is the oxidation state of the S element [53,54].

Based on the transmission line theory, the value of relative permittivity and RL of the samples can be obtained by calculating the relative permittivity and permeability of the materials measured at a given frequency and thickness of the samples [55,56]. The EMW absorption properties of NiS_2, NiS_2 and NbS_2–NiS_2 heterostructure samples have

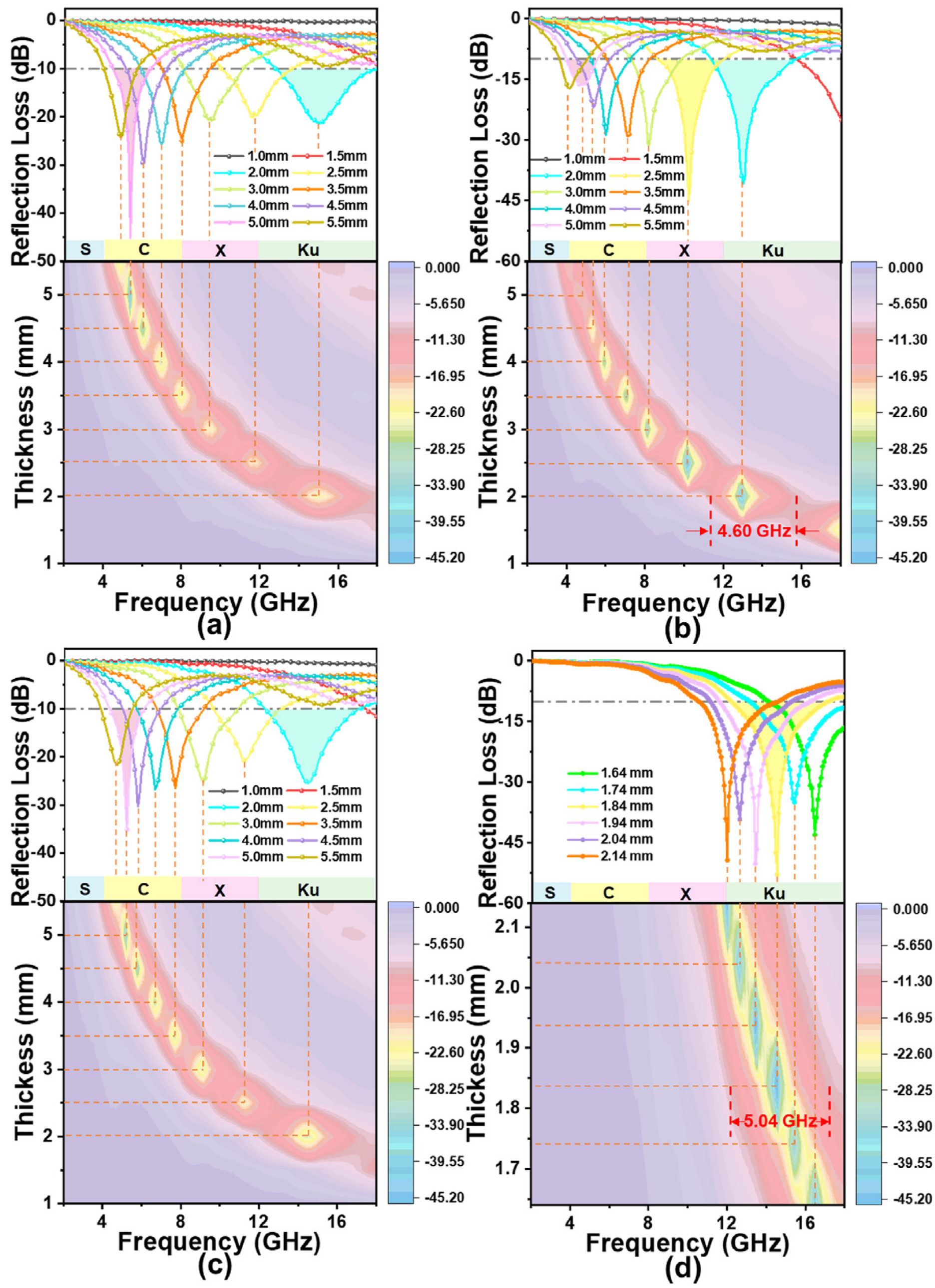

Fig. 4. RL curves for (a) NbS_2 -NiS_2-1, (b) NbS_2 -NiS_2-2, (c) NbS_2 -NiS_2-3, (d) at 2–18 GHz for NbS_2 -NiS_2-2 with a thickness of 1.64–2.14 mm.

been investigated by means of calculated RL. The RL values are obtained from Eq. (1) and the normalized input impedance (Z_{in}) of the materials from Eq. (2) can be determined [57,58]:

$$RL = 20\ log_{10}\frac{|Z_{in} - Z_0|}{|Z_{in} + Z_0|} \tag{1}$$

$$Z_{in} = Z_0\sqrt{\frac{\mu_r}{\varepsilon_r}}\tan h\left[j\frac{2\pi fd}{c}\sqrt{\mu_r\varepsilon_r}\right] \tag{2}$$

The Z_{in} in Equation (1) is the incoming resistance value and Z_0 is the free-space impedance. As in Eq. (2), ε_r ($\varepsilon_r = \varepsilon' - j\varepsilon''$)is the complex permittivity, μ_r ($\mu_r = \mu' - j\mu''$) is the magnetic permeability, the velocity of the EMW in free energy space is represented by c, and f is the frequency of the EMW, and the thickness of the material is measured by the RL. A value of RL < -10 dB indicates that the material has EMW properties and that 90% of the EMW energy will be reflected, with lower values of RL indicating higher EMW capability. The EAB is used to express the frequency scale in which materials exhibit EMW properties [59,60].

The RL values of the NbS_2–NiS_2 heterostructures with different NiS_2 loadings are shown in Fig. 4a-d and S3(a, b). It is found that the NbS_2–NiS_2 heterostructure has much better reflection loss performance than NbS_2 and NiS_2 nanoparticles, indicating that the construction of NbS_2–NiS_2 heterostructure has significantly improved its EMWL capability. Moreover, by observing the RL values of different samples at a thickness of 2.0 mm (Fig.S4), the EAB has a tendency to move to lower frequencies with the increase of NiS_2 loading. It is shown that the construction of NbS_2–NiS_2 homogeneous heterophase interface not only significantly improves the EMWL capability but also contributes to the modulation of the absorption band. The reflection loss for NbS_2–NiS_2-1 is shown in Fig. 4a, with an RL_{min} of −46.7 dB at a thickness of 5.0 mm and a frequency of 5.2 GHz. NbS_2–NiS_2-2 has RL_{min} values of −41.3 dB and −46 dB at 2.0 mm and 2.5 mm thicknesses, with EAB of 3.7 GHz (8.4–12.1 GHz) and 4.6 GHz (11.2–15.7 GHz), respectively. In addition, the minimum reflection loss reaches −20 dB at most of the sample thicknesses (1.5 mm–4.5 mm), with 99% of the microwave energy absorbed. NbS_2–NiS_2-3 has an RL_{min} value of −35 dB at a thickness of 5.0 mm and a frequency of 5.2 GHz (Fig. 4c). In addition, the performance of NbS_2–NiS_2-2 is further analyzed (Fig. 4d), and the RL_{min} can be as high as −53.1 dB at a thickness of 1.84 mm with an EAB of 5.04 GHz.

An absorption performance for microwave energy is strongly influenced by the complex dielectric constant and the complex permeability (Real part represents the stored microwave energy and the imaginary part represents the microwave energy that it could be lost). Using a coaxial measurement method (2–18 GHz), the electromagnetic parameters of our samples are determined by the tangent of the dielectric loss ($\tan\delta_E = \frac{\varepsilon''}{\varepsilon'}$) and the tangent of the magnetic loss ($\tan\delta_M = \frac{\mu''}{\mu'}$) [61,62]. Fig.S5(a-c) show μ' and μ'' for NbS_2 at different NiS_2 loadings. Since NbS_2, NiS_2 and NbS_2–NiS_2 are weakly magnetic (Fig.S6(a-c)), it is clear that the magnetic properties of NbS_2–NiS_2 hardly vary with increasing NiS_2 nanoparticle content. Fig. 5(a–c) displays the tangent of complex dielectric constant and dielectric loss for NiS_2 and NbS_2 composites. The permittivity loss can be explained by Eq. (3) and Eq. (4) in Debye's theory [63,64]:

$$\varepsilon' = \varepsilon_\infty + \frac{\varepsilon_s - \varepsilon_\infty}{1 + (2\pi f)^2 \tau^2} \tag{3}$$

$$\varepsilon'' = \frac{\varepsilon_s - \varepsilon_\infty}{1 + \omega^2\tau^2}\omega\tau + \frac{\sigma}{\omega\varepsilon_0} \tag{4}$$

In this case, the phase of the relative permittivity in the high-frequency limit is denoted by ε_∞ , ε_0 ($\varepsilon_0 = 8.854 \times 10^{-12} \bullet \mathrm{m}^{-1}$) is the vacuum permittivity, and ε_s is the stationary permittivity. The τ, ω, and σ indicate the time of polarization relaxation, the angular frequency, and the electrical conductivity, respectively.

Fig. 5a-c displays that both ε' and ε'' of the materials are frequency-dependent, and the value of ε of the NbS_2–NiS_2 heterostructure decreases with increasing frequency. on the theory of free electrons, the electrical permittivity of the hybrid material increases with increasing frequency, while ε decreases as frequency increases. As a result of electromagnetic fields, the random dipole of the sample changes its direction to be parallel to the external fields, resulting in relaxation of the polarization and is required to overcome the resistance during the energy loss. Since the dipoles can't follow the speed of the outside electromagnetic frequency field when the frequency is higher than a certain value, which do not contribute much to the dielectric polarization, rearrangements occur leading to a gradual decrease in dielectric response with increasing frequency. Due to the NbS_2 and NiS_2 structures have different conductivities, the mismatch of conductivity results in the concentration of charge and polarization of the interface. Mismatch between the two structures leads to lattice defects in the interfacial region, which result in a significant increase of ε after the introduction of NiS_2. When the loading of NiS_2 exceeds a critical value, the homogeneous phase of the material is broken, and an aggregated structure shown in Fig. 5d is formed. As a result, the high energy barrier could be established at the interface, leading to a significant reduction of the free-electron transport at the interface.

The dielectric loss type can be identified by means of a Cole-Cole shape. When Debye slackening occurs, ε'' versus ε' shows semicircles on the curves (Cole-Cole circles), every semi-circle matching a Debye slackening process. And such process can be described by Eq. (5) [65]:

$$\left(\varepsilon' - \frac{\varepsilon_s + \varepsilon_\infty}{2}\right)^2 + (\varepsilon'')^2 = \left(\frac{\varepsilon_s + \varepsilon_\infty}{2}\right)^2 \tag{5}$$

From Fig.S7(a, b) and Fig. 5(d–f), it can be seen that NbS_2–NiS_2-(1–3)

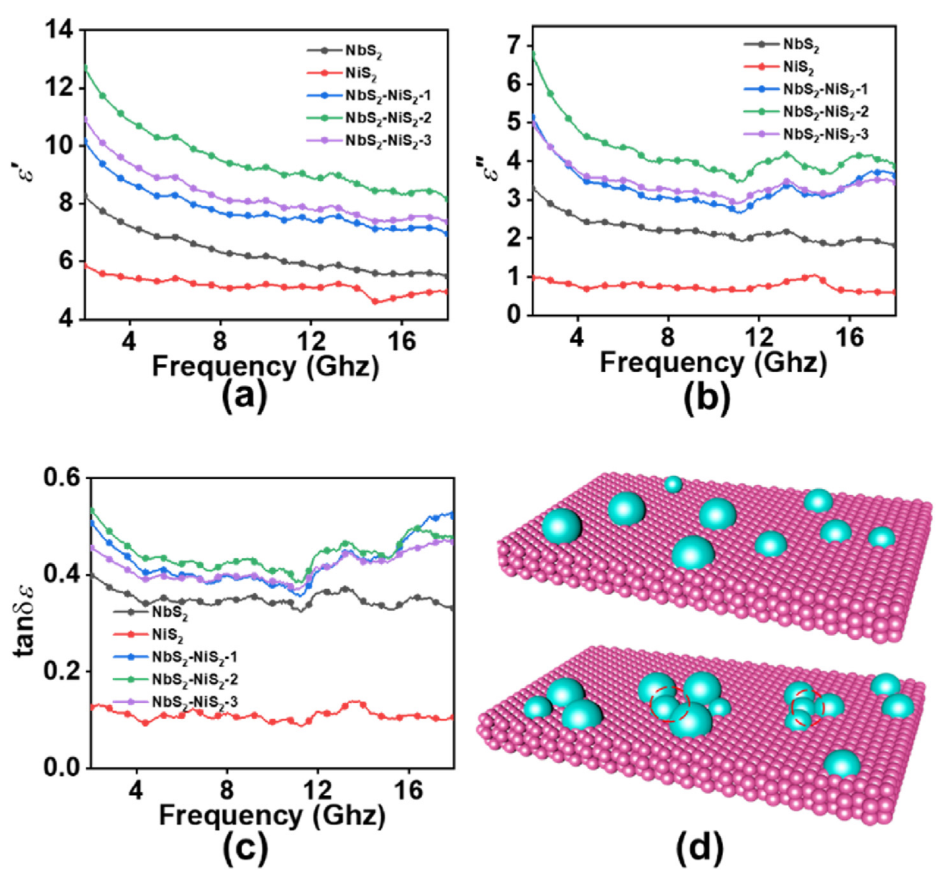

Fig. 5. Dielectric properties of the samples. (a) Real permittivity, (b) imaginary permittivity, and (c) dielectric loss tangent of NbS_2, NiS_2, and NbS_2– NiS_2. (d) Schematic illustration of electromagnetic-wave absorption mechanisms in NbS_2–NiS_2.

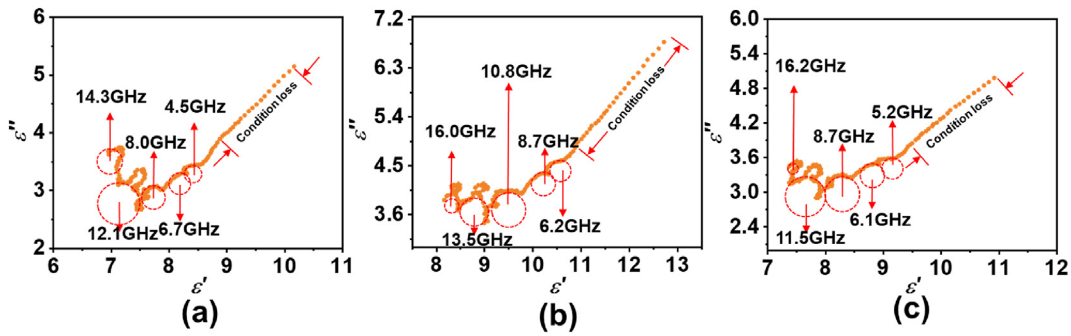

Fig. 6. The Cole-Cole plots of (a) NbS_2–NiS_2-1, (b) NbS_2–NiS_2-2, (c) NbS_2–NiS_2-3.

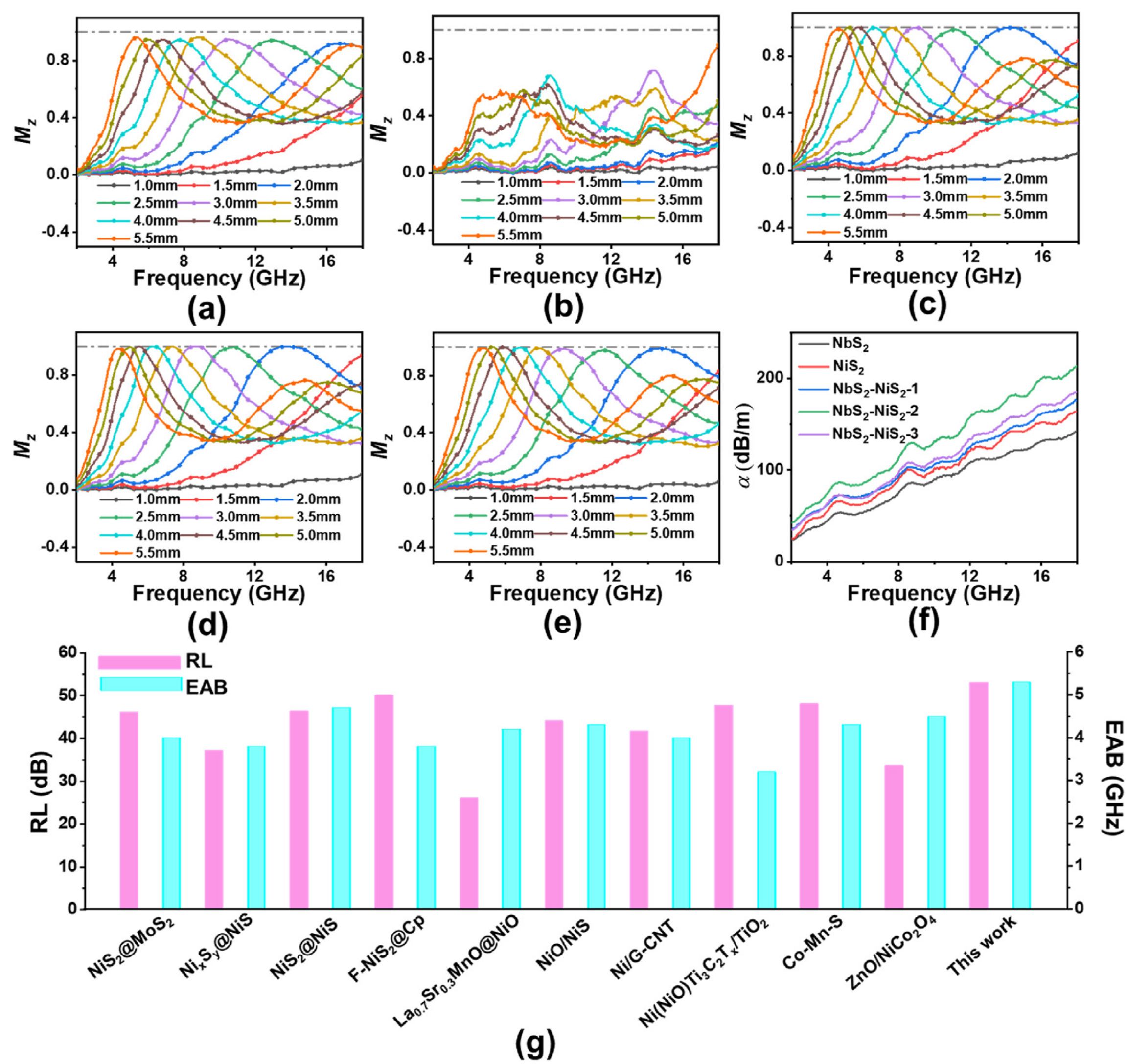

Fig. 7. Impedance matching of (a) NbS_2, (b) NiS_2, (c) NbS_2–NiS_2 -1, (d) NbS_2–NiS_2 -2, (e) NbS_2–NiS_2 -3 and (f) Attenuation constant, (g) Comprehensive Comparison of EMW absorption properties of microwave absorbing materials reported for derived Ni and based sulphide materials.

have more semicircles compared to NbS_2 and NiS_2, indicating the existence of dielectric polarization relaxation processes in NbS_2–NiS_2. The NbS_2 relaxation happens at 14.3, 12.1, 4.5 and 6.7 GHz. For NiS_2 (Fig. S7b) as shown in Fig. S7a, there are four relaxation processes at 14.6, 8.2 and 7.1 GHz respectively. The relaxation of NbS_2–NiS_2-1 (Fig. 6a) occurs at 14.3, 12.1, 8.0, 6.7 and 4.5 GHz. For the relaxation of NbS_2–NiS_2-2 (Fig. 6b), there are four relaxation processes at 16.0, 13.5, 10.8, 8.7 and 6.2 GHz and NbS_2–NiS_2-2 has a larger transmission loss. The electrical conductivity values of NbS_2, NiS_2 and NbS_2–NiS_2 are tested. The electrical conductivities of NbS_2 nano hollow spheres, NiS_2 and NbS_2–NiS_2 are 0.001 S/mm, 0.04 S/mm and 0.006 S/mm, respectively. The electrical conductivity of the NbS_2–NiS_2 heterojunction is enhanced compared to that of the NbS_2 hollow spheres. The appearance of smooth arcs on the Cole-Cole curve except for the semicircles indicates the presence of conduction losses in the material. The greater the slope of the arc the greater the corresponding conductivity will be [66–68] Due to the introduction of NiS_2 material, the phase interface of the material constitutes a low-energy-barrier homogeneous heterogeneous interface with fast response to the applied electric field, providing a unique interfacial polarization, and this low-energy barrier facilitates the electron transport on the substrate, resulting in a reduction of scattering and an improvement of conduction loss. This result is consistent with the results obtained from the tests. Some relaxation processes can be attributed to accumulation and inhomogeneous dispersion of spatial charges at the heterophane contact interface, resulting in an electric dipole moment, which rotates with the applied alternating electric field. When the rotation frequency lags behind the intrinsic frequency of the applied alternating electric field, the relaxation occurs, thus realizing the loss of electromagnetic waves. Others appearance of flaccidity peaks may be explained by defects in hydrothermal process. Therefore, the doping of NiS_2 has a significant effect on the dipolar and interface polarity of the composites and the relaxation loss and conduction loss significantly influent the dielectric loss of the samples.

It is worth noting that superior performance EMW absorbing materials require not only high dielectric losses, but also well-matched impedance (M_Z) and powerful attenuation constants (α) are necessary. Where impedance matching can be expressed by M_Z in equation (6) [69,70]:

$$M_Z = \frac{Z'_{in}}{|Z_{in}|^2 + 1} \quad (6)$$

M_Z should be adjusted to improve matching of impedances over the proper spectrum of frequencies, because when M_Z is 1, the EMW could be completely inside the materials. The impedance values of NbS_2–NiS_2 are presented in Fig. 7(a–e), which are almost equal to 1 for the samples with various thicknesses, indicating that the EMW can easily pass from the surface into the interior of the sample. The introduction of NiS_2 generates a heterogeneous structure on the surface of NbS_2. This heterogeneous structure facilitates the formation of interfaces and flaws inducing poling, which in turn affects the permittivity and achieves superior impedance matching.

If the electromagnetic wave absorber wants to have good absorbing performance, it also needs to have strong attenuation ability. The material's attenuation behavior, based on the theory of transport wires, is defined by α, as follows [71,72]:

$$\alpha = \frac{\sqrt{2}\pi f}{c} \times \sqrt{(\mu''\varepsilon'' - \mu'\varepsilon') + \sqrt{(\mu''\varepsilon'' - \mu'\varepsilon')^2 + (\varepsilon'\mu'' + \varepsilon''\mu')^2}} \quad (7)$$

The value of α is proportional to the value of the EMWL into the interior of the material. As shown in Fig. 7f, in the case of NbS_2–NiS_2-2, the α value is the maximum of all tested examples (over the frequency scale of 2–18 GHz), indicating that the microwave attenuation performance of NbS_2–NiS_2-2 is stronger than those of other samples. The results also suggest that when the EMW encounters NbS_2–NiS_2-2, they can penetrate as many surfaces as possible in the absorber, and could significantly attenuated. Therefore, NbS_2–NiS_2-2 has excellent waves absorbing characteristics, as shown by the RL curves of NbS_2–NiS_2-2.

As discussed above, construction NbS_2–NiS_2 homogeneous heterophane interface in the materials successfully improves their EML and impedance matching. Fig. 8 illustrates the schematic mechanism of NbS_2–NiS_2 absorptions. To begin with, the NbS_2–NiS_2 heterostructure has excellent electrical conductivity, and under the effect of an alternating electromagnetic field, the electrons migrate through the conductive network to absorb the electromagnetic energy, which is converted into thermal energy. Second, NbS_2 is a nano-hollow sphere made of stacked nanosheets, and its unique hollow structure promotes multiple reflections of EMW, resulting in an extended EMW travelling path, and ensuring that incident electromagnetic waves are absorbed as efficiently as possible. Thirdly, the large number of defects generated by the solvothermal synthesis of NbS_2 hollow spheres as well as the lattice distortions induced by the strong electron transfer at the heterogeneous interfaces result in a large number of randomly distributed charges aggregated at the heterogeneous interfaces, which relax under the action of an alternating electric field. Finally, due to the presence of a low potential barrier in the NbS_2–NiS_2 homogeneous heterophane interface, a specific interfacial polarization can be generated, which improves the sample's transmission loss properties and optimizes the impedance matching of the material.

3D radar cross-section (RCS) profiles of NbS_2, NbS_2–NiS_2, NiS_2, and perfect electrical conductor (PEC) were modeled by CST Microwave Studio to predict the effectiveness of NbS_2–NiS_2 for practical applications

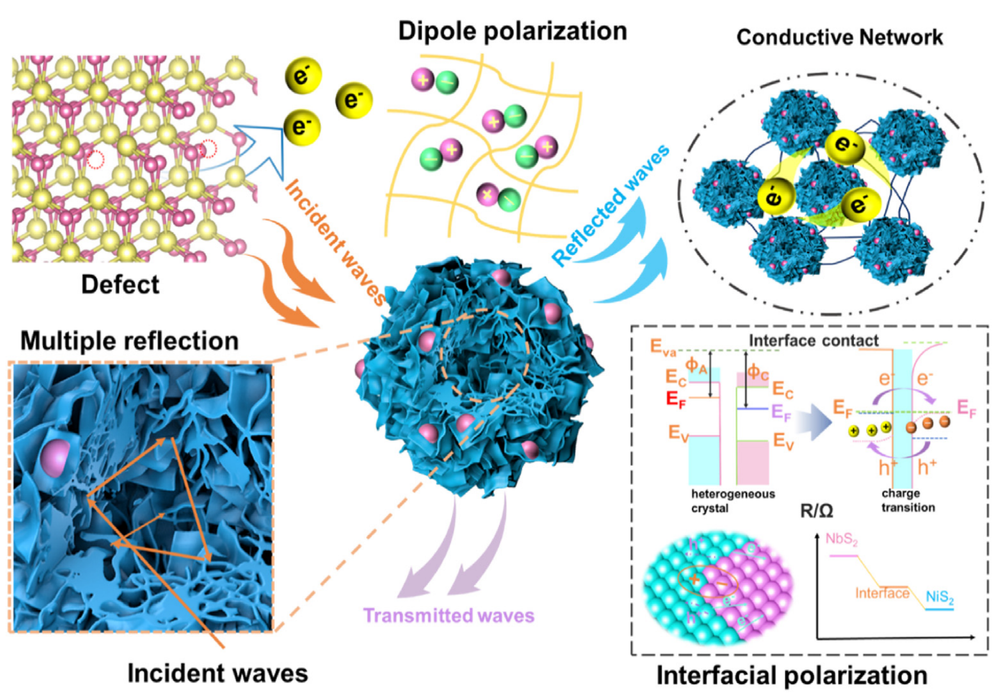

Fig. 8. Illustration of the possible EMW loss mechanisms for NbS_2–NiS_2 sample.

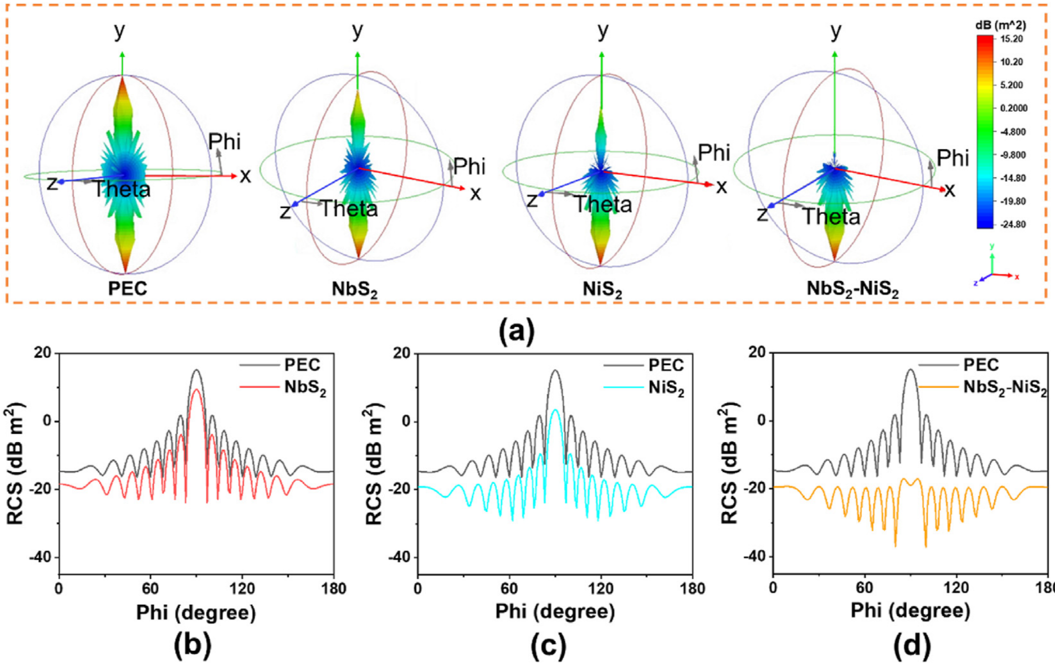

Fig. 9. (a)The far-field RCS simulation of PEC, NbS_2–NiS_2, NbS_2, NiS_2 at a coating thickness of 1.84 mm. RCS curves of (b)NbS_2–NiS_2, (c) NiS_2 and (d) NbS_2–NiS_2 samples.

as an absorber of EMW. The simulation models (200 mm × 200 mm) are the PEC and PEC coated with NbS_2, NbS_2–NiS_2 or NiS_2, respectively [60, 73]. Fig. 9a shows that the PEC plate exhibits significant scattering characteristics at different EMW incidence angles. However, the radar scattering characteristics of PEC coated with NbS_2–NiS_2 at a thickness of 1.84 mm show significant attenuation (at $0-180^{\circ}$), indicating that the EMW energy is significantly absorbed by NbS_2–NiS_2. The EMW absorption properties of PEC, NbS_2, NiS_2, NbS_2–NiS_2 can be intuitively evaluated using 2D RCS diagram distributions in the X–O–Y planes. As is shown in Fig. 9b-d, the RCS values of PEC, NbS_2, NiS_2, NbS_2–NiS_2 are 14.9, 8.2, 3.2, and -1 8.7 dB m^2. Compared with PEC, NbS_2, and NiS_2, the RSC values of NbS_2–NiS_2 decrease significantly, further indicating that NbS_2–NiS_2 has excellent EMW attenuation ability.

4. Conclusions

In summary, a novel NbS_2–NiS_2 homogeneous heterophane interface has been prepared using a continuous solvent-thermal method. The interfacial engineering strategy is viable in generating a full contact between different phases at the heterophane interface, leading to inter-interfacial polarization that could enhance the EMWL capability of the absorber. Moreover, the presence of the interfaces endows the absorber with both improved matching of impedance and enhanced dielectric losses. When the NiS_2 content is 15 wt% with a thickness of 1.84 mm, RL_{min} is −53.1 dB at 14.56 GHz with a BET of 5.04 GHz (12.15–17.19 GHz). Since the NbS_2–NiS_2 heterostructures have simple synthesis routes and excellent EMW absorption properties, the NbS_2–NiS_2 heterostructure is considered to have promising research and practical applications in electromagnetic absorption.

CRediT authorship contribution statement

Yiru Fu: Conceptualization, Investigation, Writing-original draft, Formal analysis, Methodology. Yuping Wang: Writing-original draft, Data curation, contributed to the general discussion. Junye Cheng: Data curation, Writing-review, Investigation. Yao Li: Investigation, contributed to the general discussion. Jing Wang: contributed to the general discussion. Yongheng Jin: Investigation, contributed to the general discussion. Deqing Zhang: Conceptualization, Methodology, Formal analysis. Guangping Zheng: Writing-review & editing. Maosheng Cao: Data curation, Visualization, Writing - review & editing.

Declaration of competing interest

The authors declare that they have no known competing financial interests or personal relationships that could have appeared to influence the work reported in this paper.

Acknowledgments

This work was supported by the National Natural Science Foundation of China (52372289, 52102368, 52072192 and 51977009), and Regional Joint Fund for Basic Research and Applied Basic Research of Guangdong Province (No. 2020A1515110905), Guangdong Special Fund for key Areas (20237DZX3042), Shenzhen Stable Support Project and the Fundamental Research Fund of Heilongjiang Provincial University (145309101).

Appendix A. Supplementary data

Supplementary data to this article can be found online at https://doi.org/10.1016/j.nanoms.2024.05.003.

References

[1] Z. Zhou, X. Yang, D. Zhang, H. Zhang, J. Cheng, Y. Xiong, Z. Huang, H. Wang, P. Zhang, G. Zheng, M. Cao, Achieving superior G2Hz-absorption performance in VB-group laminated VS_2 microwave absorber with dielectric and magnetic synergy effects, Adv. Compos. Hybrid Mater. 5 (2022) 2317–2327.
[2] G. Fang, C. Liu, X. Wei, Q. Cai, C. Chen, G. Xu, G. Ji, Determining the preferable polarization loss for magnetoelectric microwave absorbers by strategy of controllably regulating defects, Chem. Eng. J. 463 (2023) 142440.
[3] M. Qin, L. Zhang, H. Wu, Dielectric loss mechanism in electromagnetic wave absorbing materials, Adv. Sci. 9 (2022) e2105553.
[4] C. Liu, Z. Zeng, J. Qiao, Q. Wu, W. Liu, F. Gao, J. Liu, Versatile cellulose nanofibril assisted preparation of ultralight, scalable carbon nanotube aerogel-based electromagnetic wave absorbers with ultrahigh reflection loss, Carbon 213 (2023) 118277.

[5] J. Cheng, S. Ran, T. Li, M. Yan, J. Wu, S. Boles, B. Liu, H. Raza, S. Ullah, W. Zhang, G. Chen, G. Zheng, Achieving superior tensile performance in individual Metal−Organic framework crystals, Adv. Mater 35 (2023) 2210829.

[6] J. Ma, X. Wang, W. Cao, C. Han, H. Yang, J. Yuan, M. Cao, A facile fabrication and highly tunable microwave absorption of 3D flower-like Co_3O_4-rGO hybrid-architectures, Chem. Eng. J. 339 (2018) 487–498.

[7] M. He, J. Hu, H. Yan, X. Zhong, Y. Zhang, P. Liu, J. Kong, J. Gu, Shape anisotropic chain-like CoNi/polydimethylsiloxane composite films with excellent low-frequency microwave absorption and high thermal conductivity, Adv. Funct. Mater. (2024) 2316691.

[8] R. Xu, D. Xu, Z. Zeng, D. Liu, $CoFe_2O_4$/porous carbon nanosheet composites for broadband microwave absorption, Chem. Eng. J. 427 (2022) 130796.

[9] B. Wen, H. Yang, Y. Lin, L. Ma, Y. Qiu, F. Hu, Controlling the heterogeneous interfaces of S, Co co-doped porous carbon nanosheets for enhancing the electromagnetic wave absorption, J. Colloid Interface Sci. 586 (2021) 208–218.

[10] D. Jia, X. Li, R. Cai, B. Ma, Q. Zhao, T. Chigan, P. Yang, Interfacial covalent bonding of Ni doped MoS_2/TiO_2/$Ti_3C_2T_x$ composites for electromagnetic wave absorption performance, Appl. Surf. Sci. 638 (2023) 158116.

[11] F. Pan, Y. Shi, Y. Yang, H. Guo, L. Li, H. Jiang, X. Wang, Z. Zeng, W. Lu, Porifera-Inspired lightweight, thin, wrinkle-resistance, and multifunctional MXene foam, Adv. Mater. (2024) 2311135.

[12] J. Ma, S. Fan, J. Wang, Q. Zheng, L. Wang, W. Jiang, Sequential-etching assisted construction of Co_3O_4/N-doped carbon@$CoNi_x$ yolk-shelled heterostructures with dual loss sites for highly efficient electromagnetic wave absorption, Chem. Eng. J. 442 (2022) 136394.

[13] B. Schuler, D.Y. Qiu, S. Refaely-Abramson, C. Kastl, C.T. Chen, S. Barja, R.J. Koch, D.F. Ogletree, S. Aloni, A.M. Schwartzberg, J.B. Neaton, S.G. Louie, A. Weber-Bargioni, Large spin-orbit splitting of deep in-gap defect states of engineered sulfur vacancies in monolayer WS_2, Phys. Rev. Lett. 123 (2019) 076801.

[14] S. Ippolito, A.G. Kelly, R. Furlan de Oliveira, M.-A. Stoeckel, D. Iglesias, A. Roy, C. Downing, Z. Bian, L. Lombardi, Y.A. Samad, V. Nicolosi, A.C. Ferrari, J.N. Coleman, P. Samorì, Covalently interconnected transition metal dichalcogenide networks via defect engineering for high-performance electronic devices, Nat. Nanotechnol. 16 (2021) 592–598.

[15] B. Du, M. Cai, X. Wang, J. Qian, C. He, A. Shui, Enhanced electromagnetic wave absorption property of binary ZnO/$NiCo_2O_4$ composites, J. Adv. Ceram. 10 (2021) 832–842.

[16] J. Zhao, Z. Gu, Q. Zhang, Stacking MoS_2 flower-like microspheres on pomelo peels-derived porous carbon nanosheets for high-efficient X-band electromagnetic wave absorption, Nano Res. 18 (2023), 1998-0124.

[17] B. Li, H. Tian, L. Li, W. Liu, J. Liu, Z. Zeng, N. Wu, Graphene-Assisted assembly of electrically and magnetically conductive ceramic nanofibrous aerogels enable multifunctionality, Adv. Funct. Mater. (2024) 2314653.

[18] Y. Li, Y. Jin, J. Cheng, Y. Fu, J. Wang, L. Fan, D. Zhang, P. Zhang, G. Zheng, M. Cao, Achieving superior electromagnetic wave absorbers with 2D/3D heterogeneous structures through the confinement effect of reduced graphene oxides, Carbon 213 (2023) 118245.

[19] F. Cardoso Ofredi Maia, I.O. Maciel, D. Vasconcelos Pazzini Massote, B.S. Archanjo, C. Legnani, W.G. Quirino, V. Carozo Gois de Oliveira, B. Fragneaud, Defect activated optical Raman modes in single layer $MoSe_2$, Nanotechnology 32 (2021) 465302.

[20] J. Liang, S. Li, F. Li, L. Zhang, Y. Jiang, H. Ma, K. Cheng, L. Qing, Defect engineering induces Mo-regulated Co_9Se_8/FeNiSe heterostructures with selenium vacancy for enhanced electrocatalytic overall water splitting in alkaline, J. Colloid Interface Sci. 655 (2024) 296–306.

[21] C. Witteveen, K. Gornicka, J. Chang, M. Mansson, T. Klimczuk, F.O. von Rohr, Polytypism and superconductivity in the NbS_2 system, Dalton Trans. 50 (2021) 3216–3223.

[22] Z. Gao, D. Lan, L. Zhang, H. Wu, Simultaneous manipulation of interfacial and defects polarization toward Zn/Co phase and ion hybrids for electromagnetic wave absorption, Adv. Funct. Mater. 31 (2021) 2106677.

[23] S. Lim, S. Pan, K. Wang, A.V. Ushakov, E.V. Sukhanova, Z.I. Popov, D.G. Kvashnin, S.V. Streltsov, S.W. Cheong, Tunable single-atomic charges on a cleaved intercalated transition metal dichalcogenide, Nano Lett. 22 (2022) 1812–1817.

[24] J. Cheng, X. Yang, L. Dong, Z. Yuan, W. Wang, S. Wu, S. Chen, G. Zheng, W. Zhang, D. Zhang, H. Wang, Effective nondestructive evaluations on UHMWPE/Recycled-PA6 blends using FTIR imaging and dynamic mechanical analysis, Polym. Test. 59 (2017) 371–376.

[25] X. Zhang, X.-L. Tian, Y. Qin, J. Qiao, F. Pan, N. Wu, C. Wang, S. Zhao, W. Liu, J. Cui, Z. Qian, M. Zhao, J. Liu, Z. Zeng, Conductive metal–organic frameworks with tunable dielectric properties for boosting electromagnetic wave absorption, ACS Nano 17 (2023) 12510–12518.

[26] Y. Zhang, G. Xu, G. Lian, F. Luo, Q. Xie, Z. Lin, G. Chen, Electrochemiluminescence biosensor for miRNA-21 based on toehold-mediated strand displacement amplification with $Ru(phen)_3^{2+}$ loaded DNA nanoclews as signal tags, Biosens. Bioelectron. 147 (2020) 111789.

[27] H. Zhang, T. Liu, Z. Huang, J. Cheng, H. Wang, D. Zhang, X. Ba, G. Zheng, M. Yan, M. Cao, Engineering flexible and green electromagnetic interference shielding materials with high performance through modulating WS_2 nanosheets on carbon fibers, J. Materiomics 8 (2022) 327–334.

[28] D. Zhang, H. Wang, J. Cheng, C. Han, X. Yang, J. Xu, G. Shan, G. Zheng, M. Cao, Conductive WS_2-NS/CNTs hybrids based 3D ultra-thin mesh electromagnetic wave absorbers with excellent absorption performance, Appl. Surf. Sci. 528 (2020) 147052.

[29] Z. Huang, J. Cheng, H. Zhang, Y. Xiong, Z. Zhou, Q. Zheng, G. Zheng, D. Zhang, M. Cao, High-performance microwave absorption enabled by Co_3O_4 modified VB-group laminated VS_2 with frequency modulation from S-band to Ku-band, J. Mater. Sci. Technol. 107 (2022) 155–164.

[30] S. Ippolito, P. Samorì, Defect engineering strategies toward controlled functionalization of solution-processed transition metal dichalcogenides, Small Sci. 2 (2022) 202100122.

[31] P. Wu, X. Kong, Y. Feng, W. Ding, Z. Sheng, Q. Liu, G. Ji, Phase engineering on amorphous/crystalline γ-Fe_2O_3 nanosheets for boosting dielectric loss and high-performance microwave absorption, Adv. Funct. Mater. (2023) 2311983.

[32] D. Zhang, S. Liang, J. Chai, T. Liu, X. Yang, H. Wang, J. Cheng, G. Zheng, M. Cao, Highly effective shielding of electromagnetic waves in MoS_2 nanosheets synthesized by a hydrothermal method, J. Phys. Chem. Solid. 134 (2019) 77–82.

[33] X.-J. Zhang, S.-W. Wang, G.S. Wang, Z. Li, A.-P. Guo, J.Q. Zhu, D.P. Liu, P.G. Yin, Facile synthesis of NiS_2@MoS_2 core–shell nanospheres for effective enhancement in microwave absorption, RSC Adv. 7 (2017) 22454–22460.

[34] Y. Zhang, H. Si, H. Liu, Z. Jiang, A. Li, M. Liu, C. Gong, Heterogeneous and hierarchical ni/C/SiO_2 composite with tunable electromagnetic wave absorption, Mater. Today Phys. 36 (2023) 101149.

[35] Y. Ruan, H. Xu, H. Lei, W. Xue, T. Wang, S. Song, Y. Yu, G.-R. Zhang, D. Mei, Dendritic NiS_2@Co–N–C nanoarchitectures as bifunctional electrocatalysts for long-life Zn–air batteries, Inorg. Chem. Front. 10 (2023) 2370–2379.

[36] J. Cheng, K. Liu, X. Li, L. Huang, J. Liang, G. Zheng, G. Shan, Nickel-metal-organic framework nanobelt based composite membranes for efficient Sr^{2+} removal from aqueous solution, Environ. Sci. Technol. 3 (2020) 100035.

[37] H. Cheng, Y. Pan, W. Li, C. Liu, C. Shen, X. Liu, C. Pan, Facile design of multifunctional melamine foam with Ni-anchored reduced graphene oxide/MXene as highly efficient microwave absorber, Nano Today 52 (2023) 101958.

[38] T. Wang, P. Chang, Z. Sun, X. Wang, J. Tao, L. Guan, Interface prompted highly efficient hydrogen evolution of MoS_2/CoS_2 heterostructures in a wide pH range, Phys. Chem. Chem. Phys. 25 (2023) 13966–13977.

[39] J. Cheng, K. Liu, X. Li, L. Huang, J. Liang, G. Zheng, G. Shan, Nickel-metal-organic framework nanobelt based composite membranes for efficient Sr2+ removal from aqueous solution, Environ. Sci. Ecotechnol. 3 (2020) 100035.

[40] J. Cheng, S. Ran, T. Li, M. Yan, J. Wu, S. Boles, B. Liu, H. Raza, S. Ullah, W. Zhang, G. Chen, G. Zheng, Achieving superior tensile performance in individual metal-organic framework crystals, Adv. Mater. (2023) 2210829.

[41] B. Li, N. Wu, Q. Wu, Y. Yang, F. Pan, W. Liu, J. Liu, Z. Zeng, From "100%" utilization of MAX/MXene to direct engineering of wearable, multifunctional E-textiles in extreme environments, Adv. Funct. Mater. 33 (2023) 2307301.

[42] B. Li, M. Liu, W. Zhong, J. Xu, X. Zhang, X. Zhang, X. Zhang, Y. Chen, Partially contacted NixSy@N, S-codoped carbon yolk-shelled structures for efficient microwave absorption, Carbon 182 (2021) 276–286.

[43] H. Zhang, J. Cheng, H. Wang, Z. Huang, Q. Zheng, G. Zheng, D. Zhang, R. Che, M. Cao, Initiating VB-group laminated NbS_2 electromagnetic wave absorber toward superior absorption bandwidth as large as 6.48 GHz through phase engineering modulation, Adv. Funct. Mater. 32 (2021) 2108194.

[44] S. Wang, L. Zhao, J. Li, X. Tian, X. Wu, L. Feng, High valence state of Ni and Mo synergism in NiS_2-MoS_2 hetero-nanorods catalyst with layered surface structure for urea electrocatalysis, J. Energy Chem. 66 (2022) 483–492.

[45] Z. Yang, B. Wang, Y. Chen, W. Zhou, H. Li, R. Zhao, X. Li, T. Zhang, F. Bu, Z. Zhao, W. Li, D. Chao, D. Zhao, Activating sulfur oxidation reactionviasix-electron redox mesocrystal NiS_2 for sulfur-based aqueous batteries, Natl. Sci. Rev. 10 (2023) nwac268.

[46] M. Chen, Y. Zhang, R. Wang, B. Zhang, B. Song, Y. Guan, S. Li, P. Xu, Surface reconstruction of Se-doped NiS_2 enables high-efficiency oxygen evolution reaction, J. Energy Chem. 84 (2023) 173–180.

[47] Y. Zhang, L. Yin, J. Chu, T.A. Shifa, J. Xia, F. Wang, Y. Wen, X. Zhan, Z. Wang, J. He, Edge-epitaxial growth of 2D NbS_2-WS_2 lateral metal-semiconductor heterostructures, Adv Mater (2018) e1803665.

[48] M. Zhou, S. Tan, J. Wang, Y. Wu, L. Liang, G. Ji, Three-in-One Multi-Scale Structural Design of Carbon Fiber-Based Composites for Personal Electromagnetic Protection and Thermal Management, Nano-Micro Lett. 15 (2023) 20525–20536.

[49] T. Yi, Y. Li, S. Qi, P. Peng, Y. Zhu, Y. Xie, Construction of Porous ZnS@Co_3S_4@NiO Nanosheets hybrid materials for high-performance pseudocapacitor electrode by morphology reshaping, Adv. Sustain. Syst. 4 (2020) 2000090.

[50] C. Karakaya, N. Solati, U. Savacı, E. Keleş, S. Turan, S. Çelebi, S. Kaya, Mesoporous thin-film NiS_2 as an idealized pre-electrocatalyst for a hydrogen evolution reaction, ACS Catal. 10 (2020) 15114–15122.

[51] S. Hu, C. Xiang, Y. Zou, F. Xu, L. Sun, Synthesis of $NiMoO_4$/NiMo@NiS nanorods for efficient hydrogen evolution reactions in electrocatalysts, Nanomaterials 13 (2023) 1871.

[52] Z.-L. Hou, X. Gao, J. Zhang, G. Wang, A perspective on impedance matching and resonance absorption mechanism for electromagnetic wave absorbing, Carbon 222 (2024) 118313.

[53] J. Xu, L. Liu, X. Zhang, B. Li, C. Zhu, S. Chou, Y. Chen, Tailoring electronic properties and polarization relaxation behavior of MoS_2 monolayers for electromagnetic energy dissipation and wireless pressure micro-sensor, Chem. Eng. J. 425 (2021) 131700.

[54] L. Liang, R. Yu, S.J.H. Ong, Y. Yang, B. Zhang, G. Ji, Z.J. Xu, An adaptive multispectral mechano-optical system for multipurpose applications, ACS Nano 17 (2023) 12409–12421.

[55] Z.L. Hou, X. Ma, J. Zhang, C. Li, Y. Wang, M. Cao, Fascinating electrical transport behavior of topological insulator Bi_2Te_3 nanorods: toward electrically responsive smart materials, Small 18 (2022) 176.

[56] X. Chen, S. Guo, S. Tan, J. Ma, T. Xu, Y. Wu, G. Ji, An environmentally friendly chitosan-derived VO_2/carbon aerogel for radar infrared compatible stealth, Carbon 213 (2023) 12409–12421.

[57] Z. Ma, M. Liu, B. Li, F. Yan, Y. Chen, X. Zhang, C. Zhu, Hierarchically nitrogen-doped carbon hollow microspheres assembled with loose and porous magnetic carbon sheets for enhanced microwave absorption, Carbon 212 (2023) 118165.
[58] C.-J. Li, X. Wang, X. Liu, J. Zhang, S. Bi, Z.-L. Hou, Broadband and strong microwave absorption combining excellent EMI shielding of VGCF/carbonyl iron composites derived from synergistic magnetic and dielectric losses, Carbon 214 (2023) 118383.
[59] X. Guan, S. Tan, L. Wang, Y. Zhao, G. Ji, Electronic modulation strategy for mass-producible ultrastrong multifunctional biomass-based fiber aerogel devices: interfacial bridging, ACS Nano 17 (2023) 20525–20536.
[60] C. Wen, X. Li, R. Zhang, C. Xu, W. You, Z. Liu, B. Zhao, R. Che, High-density anisotropy magnetism enhanced microwave absorption performance in $Ti_3C_2T_x$ MXene@Ni microspheres, ACS Nano 16 (2022) 1150–1159.
[61] B. Huang, M.A. McGuire, A.F. May, D. Xiao, P. Jarillo-Herrero, X. Xu, Emergent phenomena and proximity effects in two-dimensional magnets and heterostructures, Nat. Mater. 19 (2020) 1276–1289.
[62] S. Zhang, D. Lan, X. Chen, Y. Gu, J. Ren, S. Du, S. Cai, X. Zhao, Z. Zhao, G. Wu, Three-dimensional macroscopic absorbents: from synergistic effects to advanced multifunctionalities, Nano Res. 14 (2023) 12274.
[63] Y. Hou, Z. Sheng, C. Fu, J. Kong, X. Zhang, Hygroscopic holey graphene aerogel fibers enable highly efficient moisture capture, heat allocation and microwave absorption, Nat. Commun. 13 (2022) 1227.
[64] A. Elhassan, I. Abdalla, J. Yu, Z. Li, B. Ding, Microwave-assisted fabrication of sea cucumber-like hollow structured composite for high-performance electromagnetic wave absorption, Chem. Eng. J. 392 (2020) 123646.
[65] L. Chen, Y. Li, B. Zhao, S. Liu, H. Zhang, K. Chen, M. Li, S. Du, F. Xiu, R. Che, Z. Chai, Q. Huang, Multiprincipal element M_2FeC ($M = Ti,V,Nb,Ta,Zr$) MAX phases with synergistic effect of dielectric and magnetic loss, Adv. Sci. 10 (2023) e2206877.
[66] W. Wei, Z. Guo, J. Xu, Z. Fang, J. Zhang, Y. Jia, L. Mi, Novel Ni_3S_4/NiS/NC composite with multiple heterojunctions synthesized through space-confined effect for high-performance supercapacitors, Int. J. Extrem. Manuf. 5 (2022) 015504.
[67] D. Zhang, T. Liu, M. Zhang, H. Zhang, X. Yang, J. Cheng, J. Shu, L. Li, M. Cao, Confinedly growing and tailoring of Co_3O_4 clusters-WS_2 nanosheets for highly efficient microwave absorption, Nanotechnology 31 (2020) 325703.
[68] L. Wang, X. Yu, M. Huang, W. You, Q. Zeng, J. Zhang, X. Liu, M. Wang, R. Che, Orientation growth modulated magnetic-carbon microspheres toward broadband electromagnetic wave absorption, Carbon 172 (2021) 516–528.
[69] Z.-L. Hou, K. Du, Y. Zhang, S. Bi, J. Zhang, Nanoarchitectonics of MnO_2 nanotubes as sea urchin-like aggregates for dielectric response and microwave absorption with a wide concentration domain, Nano Res. 16 (2022) 2604–2610.
[70] Y. Zhang, J. Zhang, X. Wang, Z.-H. Liu, S. Bi, Z.-L. Hou, Metal-organic frameworks derived carbon nanotube and carbonyl iron composite materials for broadband microwave absorbers with a wide filling range, J. Magn. Magn Mater. 555 (2022).
[71] T. Zhao, T. Zheng, D. Lan, Y. Zhang, Z. Sun, C. Wang, Z. Jia, G. Wu, Self-assembly tungsten selenide hybrid ternary MOF derived magnetic alloys via multi-polarization to boost microwave absorption, Nano Res. 4 (2023) 12274.
[72] Z. Tang, L. Xu, C. Xie, L. Guo, L. Zhang, S. Guo, J. Peng, Synthesis of $CuCo_2S_4$@ Expanded Graphite with crystal/amorphous heterointerface and defects for electromagnetic wave absorption, Nat. Commun. 14 (2023) 5951.
[73] J. Cheng, Y. Jin, J. Zhao, Q. Jing, B. Gu, J. Wei, S. Yi, M. Li, W. Nie, Q. Qin, D. Zhang, G. Zheng, R. Che, From VIB- to VB-group transition metal disulfides: structure engineering modulation for superior electromagnetic wave absorption, Nano-Micro Lett. 16 (2023).